Research Square

Preprints are preliminary reports that have not undergone peer review.
They should not be considered conclusive, used to inform clinical practice,
or referenced by the media as validated information.

Ultrafast proton transport phosphate for protonic ceramic electrolysis cells oxygen electrodes

Zhenhua Wang

wangzh@bit.edu.cn

Beijing Institute of Technology https://orcid.org/0000-0003-3476-0924

Chenhe Jia

Beijing Institute of Technology

Rongzheng Ren

Beijing Institute of Technology

Cheng Zou

Beijing Institute of Technology

Yuanyuan Lei

Beijing Institute of Technology

Pengbo Guo

Beijing Institute of Technology

Linlin Song

Beijing Institute of Technology

Xiaodan Yu

Beijing Institute of Technology

Wang Sun

Beijing Institute of Technology

Jinshuo Qiao

Beijing Institute of Technology

Kening Sun

Beijing Institute of Technology

Article

Keywords: protonic ceramic electrolysis cells, oxygen electrodes, proton transport, phosphate

Posted Date: August 20th, 2026

DOI: https://doi.org/10.21203/rs.3.rs-10593314/v1

License: This work is licensed under a Creative Commons Attribution 4.0 International License.
Read Full License

Additional Declarations: There is **NO** Competing Interest.

Ultrafast proton transport phosphate for protonic ceramic electrolysis cells oxygen electrodes

Chenhe Jia, Rongzheng Ren, Cheng Zou, Yuanyuan Lei, Pengbo Guo, Linlin Song, Xiaodan Yu, Wang Sun, Jinshuo Qiao, Zhenhua Wang*, Kening Sun**

Beijing Key Laboratory of Green Hydrogen and Fuel Cells, School of Chemistry and Chemical Engineering, Beijing Institute of Technology, Beijing 100081, China

E-mail: renrongzheng@bit.edu.cn, wangzh@bit.edu.cn, sunkn@bit.edu.cn

Keywords: protonic ceramic electrolysis cells; oxygen electrodes; proton transport; phosphate

Abstract

Protonic ceramic electrolysis cells can directly produce dry, pressurized green hydrogen at intermediate temperatures with an energy conversion efficiency approaching 100%, but slow proton transport in oxygen electrodes limits their large-scale deployment. The coupling between oxygen vacancy hydration and proton trapping fundamentally limits proton transport in perovskite oxides. Here we introduce $Sr_3(PO_4)_2$ (SPO), a phosphate built from PO_4 tetrahedra, into perovskite oxygen electrodes. Protons migrate between neighboring tetrahedra rapidly with a calculated barrier of only 0.15 eV. This phosphate pathway is independent of the perovskite host lattice and increases the proton chemical diffusion coefficient of SFM by nearly one order of magnitude. The in situ self-assembly of SPO increases the electrolysis current density by up to 148% at 600 °C, and the best electrode achieves a current density of 2 A cm^{-2} at 600 °C and 1.3 V. Furthermore, this strategy demonstrates good universality for enhancing the performance of PCEC oxygen electrodes.

Main

Green hydrogen plays an important role in building a clean, low-carbon, secure and efficient energy system[1, 2]. Protonic ceramic electrolysis cells (PCECs) offer a promising route to hydrogen production by water electrolysis due to their unparalleled energy conversion efficiency, feasible integration with other energy sources, and direct production of dry, pressurized hydrogen[3, 4, 5]. However, the mature application of PCECs at scale has been limited due to the shortage of suitable oxygen electrode materials[6, 7]. The oxygen electrode splits water into ions and electrons, which are subsequently transported through the lattice. The rates of proton and electron transport directly affect the water splitting reaction[8]. Compared with electronic transport, proton transport depends more strongly on local lattice geometry and O–H bonding, thus governing the sluggish kinetics of the oxygen electrode reaction[9]. Constructing fast proton transport pathways within the oxygen electrode is therefore essential for improving PCEC performance.

Conventionally, proton transport in ABO_3-type perovskite oxygen electrodes relies on the hydration reaction between H_2O and oxygen vacancies, during which protons hop between adjacent lattice oxygen ions via O–H bond reorientation within the BO_6 octahedra[10, 11]. Under this mechanism, proton incorporation and subsequent transport remain coupled to oxygen vacancy chemistry[12]. Consequently, the classical approach to enhancing proton mobility involves introducing lower-valence acceptor dopants at the B sites to increase both the oxygen vacancy concentration and the extent of hydration interactions[13, 14, 15]. However, acceptor doping inevitably introduces negatively charged sites into the oxide lattice, which electrostatically associate with positively charged protonic defects, thereby creating local proton traps (Fig. 1a)[16]. As a result, oxygen vacancy formation becomes closely coupled with proton trapping, fundamentally restricting long-range proton migration[17]. Numerous strategies have been proposed to overcome this intrinsic limitation, such as tuning the oxide lattice, modulating the local electronic structure, or adjusting the oxygen vacancy concentration[18, 19]. Despite these attempts, the structural root cause of proton trapping remains unaddressed, and proton transport is still confined within the same oxide framework.

Here we introduce a vancacy-independent $Sr_3(PO_4)_2$ (SPO) into perovskite oxygen electrodes to establish an ultrafast proton transport pathway (Fig. 1b). In situ spectroscopic and spectrometric measurements, synchrotron measurements, isotope tracing and density functional theory calculations show that the PO_4 tetrahedral framework provides a homogeneous sublattice environment free of proton trapping. Protons migrate rapidly between oxygen atoms on neighboring PO_4 tetrahedra. Through in situ self assembly, we incorporated SPO into four

perovskite oxygen electrodes: $Sr_2Fe_{1.5}Mo_{0.5}O_{6-\delta}$ (SFM), $SrFe_{0.9}Nb_{0.1}O_{3-\delta}$ (SFN), $SrCo_{0.5}Fe_{0.5}O_{3-\delta}$ (SCF) and $SrCo_{0.9}Nb_{0.1}O_{3-\delta}$ (SCN)[20, 21]. At 600 °C, the in situ self-assembly of SPO reduced polarization resistance by up to 57% and increased electrolysis current density by up to 148%. The best-performing oxygen electrode (SCN-SPO) delivered an electrolysis current density of 2 A cm^{-2} at 600 °C and 1.3 V.

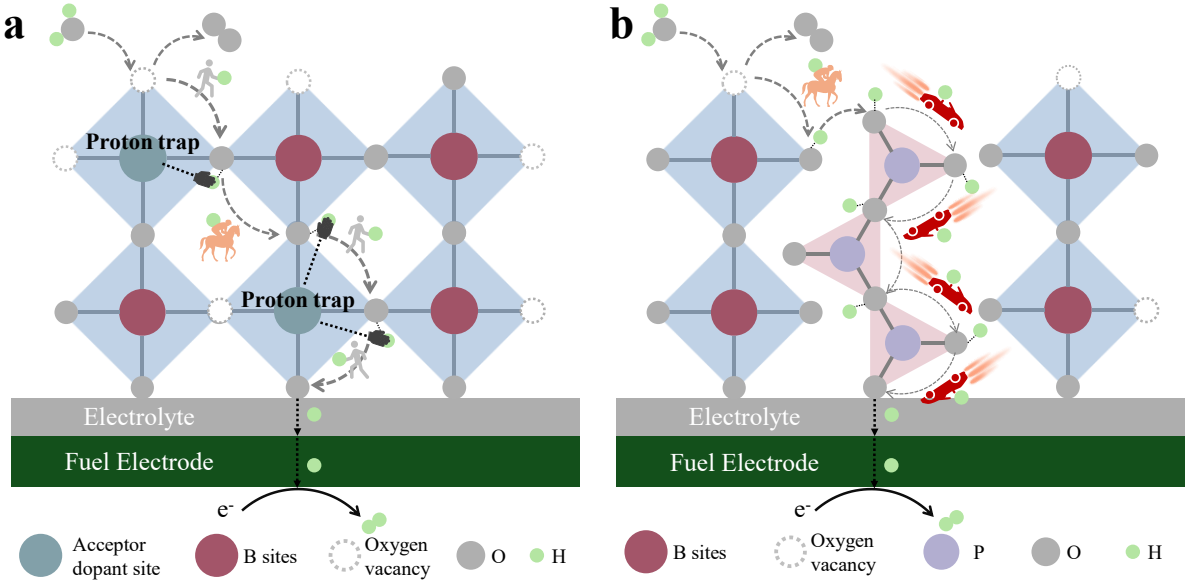


Fig. 1 | Proton transport in SPO independent of oxygen vacancies. a, Proton incorporation and transport in a conventional acceptor doped perovskite, where acceptor defects electrostatically associate with protonic defects. b, Proton transport through the PO_4 tetrahedral sublattice of SPO without structural oxygen vacancies or charged acceptor defects.

In situ assembly of a PO_4 tetrahedral phase within a BO_6 octahedral perovskite oxygen electrode

The incorporation of $Sr_3(PO_4)_2$ (SPO) into $Sr_2Fe_{1.5}Mo_{0.5}O_{6-\delta}$ (SFM) perovskite oxygen electrode was achieved by an in situ assembly stragety (Methods). SFM was selected as the initial host because it is a representative perovskite oxygen electrode with a BO_6 octahedral framework. Cubic SFM consists of a corner sharing $(Fe,Mo)O_6$ octahedral network, whereas rhombohedral SPO contains isolated PO_4 tetrahedra coordinated by Sr ion (Fig. 2a,b)[22, 23]. Powder X-ray diffraction identified pristine SFM as a single perovskite phase. Rietveld refinement reproduced the measured pattern without detectable crystalline impurities (Fig. 2c,e). After in situ assembly, characteristic reflections from both SFM and SPO confirmed the formation of the biphasic SFM-SPO composite (Fig. 2c). Refinement assigned 90.92 wt% of the composite to cubic SFM and 9.08 wt% to rhombohedral SPO, with R_p = 5.3%, R_{wp} = 7.6% and χ^2 = 1.13 (Fig. 2d). The biphasic structure remained unchanged from 400 to 700 °C, with no additional reflections detected across this operating temperature range (Fig. 2f), confirming

its phase stability.

Scanning transmission electron microscopy (STEM) combined with elemental mapping showed how the two phases were distributed within the composite (Fig. 2g). Regions enriched in P were spatially distinct from the Fe and Mo containing SFM matrix, whereas Sr was distributed across both phases. High-resolution transmission electron microscopy (HRTEM) resolved the interface between crystalline SFM and SPO domains (Fig. 2h). Lattice spacings of 2.69 Å and 4.52 Å corresponded to the SFM (110) and SPO (101) planes, respectively. No continuous amorphous layer separated the two crystalline domains, establishing direct contact between the phosphate and perovskite phases.

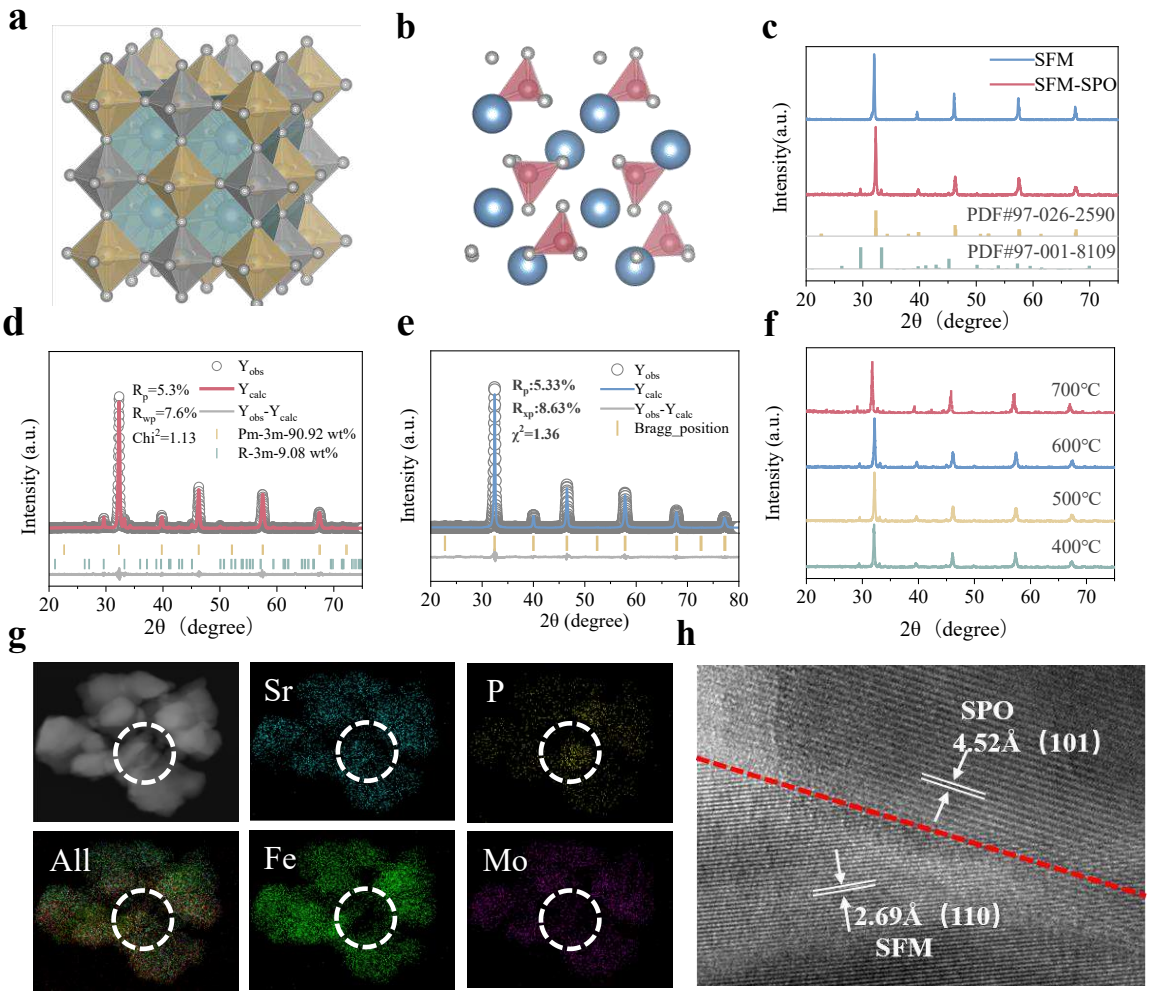


Fig. 2 | In situ assembly of a PO_4 tetrahedral phase within a BO_6 octahedral perovskite oxygen electrode. a, Crystal structure of SFM showing the BO_6 octahedral framework. b, Crystal structure of SPO showing the PO_4 tetrahedral framework. c, Powder X-ray diffraction patterns of SFM and SFM-SPO with reference reflections for SFM and SPO. d, Rietveld refinement of SFM-SPO. The refined phase fractions are 90.92 wt% cubic SFM and 9.08 wt% rhombohedral SPO. e, Rietveld refinement of pristine SFM. f, Temperature-dependent X-ray

diffraction of SFM-SPO between 400 and 700 °C. g, STEM image with Sr, P, Fe and Mo maps. h, HRTEM view of the SFM/SPO interface. The lattice spacings of 2.69 Å and 4.52 Å are assigned to the SFM (110) and SPO (101) planes, respectively.

Electrochemical performance across composite oxygen electrodes

The electrochemical performance of SFM and SFM-SPO was evaluated in symmetric cells (Supplementary Fig. S1). At 600 °C, the polarization resistance of SFM-SPO was approximately 57% lower than that of SFM (Fig. 3a,b). Arrhenius fitting yielded activation energies of 1.01 eV for SFM and 0.854 eV for SFM-SPO (Fig. 3b and Supplementary Note 1). The simultaneous reductions in polarization resistance and activation energy show that SPO accelerates the temperature dependent electrode kinetics. At matched temperatures, SFM-SPO exhibited the lowest polarization resistance among the reported SFM based oxygen electrodes (Fig. 3c and Supplementary Table S3).

The practical electrolysis performance was further evaluated in full electrolysis cells. Cross sectional microscopy showed continuous interfaces linking the porous oxygen electrode, dense electrolyte and porous fuel electrode (Supplementary Fig. S2). The SFM-SPO full electrolysis cell reached 1.25 A cm^{-2} at 600 °C and 1.3 V, representing the highest electrolysis current density reported for an SFM based oxygen electrode under comparable operating conditions (Fig. 3d-f and Supplementary Table S4). This performance also compares favourably with recently reported high performing oxygen electrodes based on other transition metal chemistries, including compositions that do not contain Fe. At 600 °C, the SFM-SPO cell produced hydrogen at a higher rate than the SFM cell from 1.3 to 1.5 V (Supplementary Fig. S4). Its Faradaic efficiency increased from approximately 63% to 79% at 1.3 V and remained higher than that of the SFM cell at 1.4 and 1.5 V (Supplementary Fig. S5 and Supplementary Note 2). The SFM-SPO cell also sustained electrolysis at 600 °C and 1.3 V for 250 h without a progressive decrease in current density (Supplementary Fig. S3). These electrolysis measurements link the lower polarization resistance to higher hydrogen production and more efficient charge utilization.

The generality of this performance improvement was demonstrated across four representative perovskite oxygen electrodes: $Sr_2Fe_{1.5}Mo_{0.5}O_{6-\delta}$ (SFM), $SrFe_{0.9}Nb_{0.1}O_{3-\delta}$ (SFN), $SrCo_{0.5}Fe_{0.5}O_{3-\delta}$ (SCF) and $SrCo_{0.9}Nb_{0.1}O_{3-\delta}$ (SCN). These materials encompass representative Co-based and Fe-based perovskite oxygen electrodes with BO_6 octahedral frameworks. For the three additional hosts, X-ray diffraction identified both the perovskite and SPO phases without additional crystalline products (Supplementary Figs. S6, S9 and S12). Impedance measurements showed lower polarization resistance for every SPO containing electrode across

the measured temperature range (Supplementary Figs. S7, S10 and S13). At 600 °C, SPO lowered the polarization resistance of SFN, SCF and SCN by 45%, 22% and 52%, respectively (Fig. 3g). Full electrolysis cells confirmed that these reductions translated into improved electrolysis performance. Relative to the corresponding unmodified electrodes, the electrolysis current densities increased by 73%, 45% and 116%, respectively (Fig. 3h and Supplementary Figs. S8, S11 and S14). These results demonstrate that the in situ self-assembly of SPO tetrahedra within conventional perovskite oxygen electrodes built from BO_6 octahedra provides a general strategy for improving electrochemical performance.

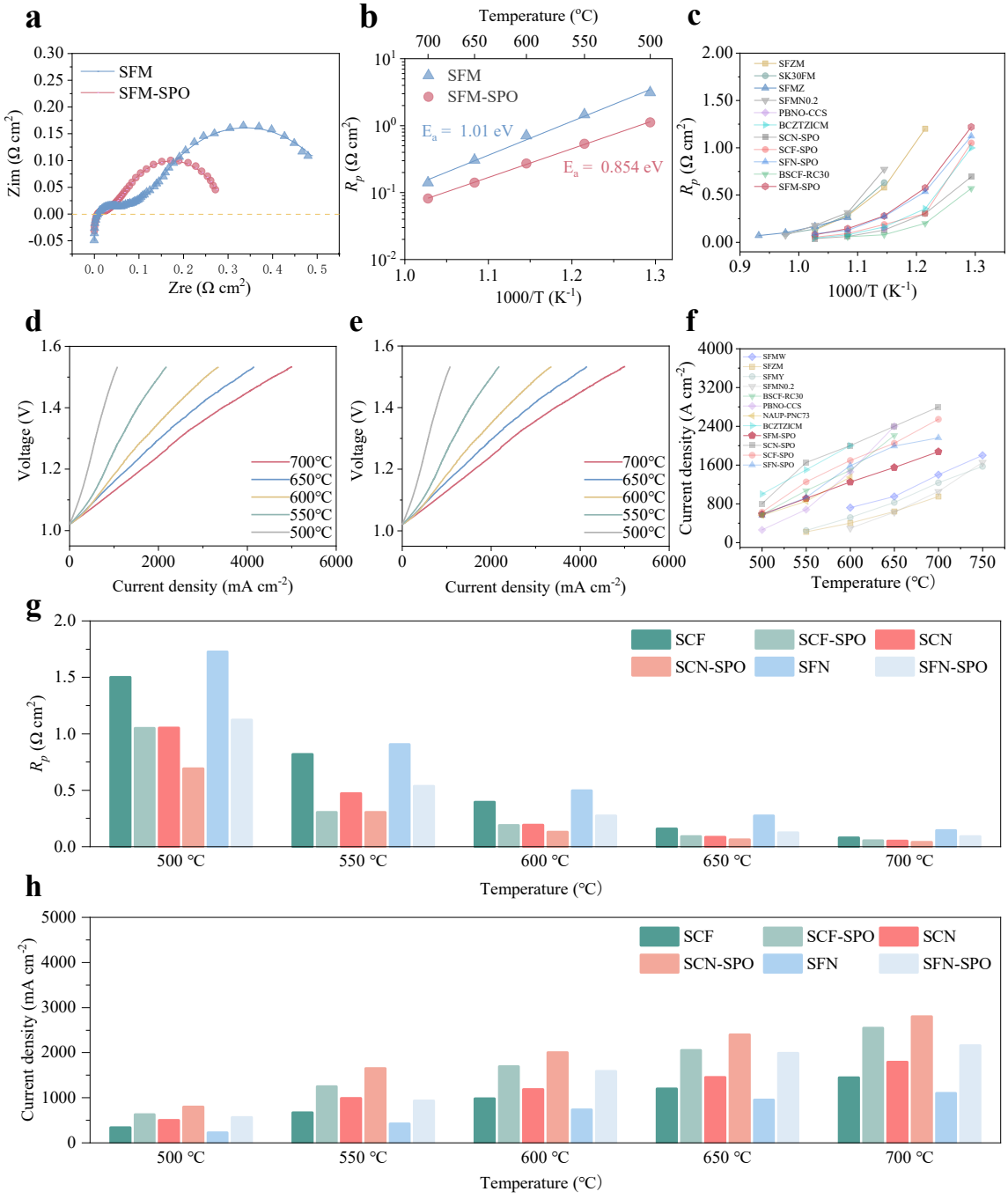


Fig. 3 | Electrochemical performance across composite oxygen electrodes. a, Impedance

spectra of SFM and SFM-SPO symmetric cells at 600 °C. b, Arrhenius plots of polarization resistance from 500 to 700 °C. c, Comparison of the polarization resistance of SFM-SPO with reported SFM-based and other high-performing oxygen electrodes. d, e, Electrolysis polarization curves of cells with SFM (d) and SFM-SPO (e) oxygen electrodes. f, Comparison of electrolysis current density with reported SFM-based and other high-performing oxygen electrodes. g, h, Polarization resistance (g) and electrolysis current density (h) of SFN, SCF and SCN before and after SPO assembly.

Selective acceleration of proton transport by SPO in the SFM composite

The oxygen electrode reaction involves two coupled processes: hydration and proton transport. Water molecules first adsorb and dissociate at oxygen vacancies to form protonic defects, after which the protons migrate between neighboring lattice oxygen ions (Fig. 4a)[11, 24, 25]. To determine the origin of the electrochemical performance enhancement, we separately examined oxygen vacancies, hydration and proton transport in SFM and SFM-SPO.

Whether SPO altered the oxygen vacancy chemistry or local structure of the SFM host was first examined by Fe K-edge X-ray absorption spectroscopy. The absorption edge of SFM-SPO shifted slightly towards lower energy relative to SFM, indicating a modest decrease in the average Fe oxidation state (Fig. 4b)[26]. This electronic adjustment was not accompanied by a reconstruction of the local Fe coordination. The principal Fe–O and higher-shell features remained at similar positions after SPO assembly (Fig. 4c)[27]. Wavelet transform maps also displayed matching Fe–O and higher shell maxima in both samples, with no additional scattering feature in SFM-SPO (Supplementary Fig. S16)[28]. EXAFS fitting gave Fe–O distances of 1.88 ± 0.02 Å for SFM and 1.90 ± 0.02 Å for SFM-SPO, with coordination numbers of 5.8 ± 1.2 and 6.1 ± 1.1, respectively, while the Fe–Sr and Fe–O–Fe distances changed by no more than 0.02 Å. The slightly higher mean Fe–O coordination number in SFM-SPO is consistent with more complete Fe–O coordination rather than oxygen vacancy enrichment (Supplementary Table S1). Thermogravimetric analysis likewise showed only a small difference in mass loss between the two samples (Supplementary Fig. S15). The preserved Fe coordination and similar water uptake exclude increased oxygen vacancy concentration or enhanced bulk hydration of SFM as the origin of the electrochemical improvement.

Hydration produced different O K-edge responses in SFM and SFM-SPO (Fig. 4d,e). In SFM, hydration attenuated the dry state feature near 533 eV and transferred intensity to approximately 534 eV, together with broader changes above 536 eV (Fig. 4e). The preedge region arises from O 2p states hybridized with Fe 3d and Mo 4d states, while the higher energy envelope contains O 2p states mixed with metal 4sp and Sr states[25]. These changes reflect

oxygen vacancy filling, O–H formation and the accompanying redistribution of the Fe/Mo–O electronic states. SFM-SPO showed an additional phosphate related response. Hydration increased the intensity between 531 and 533 eV, suppressed the feature near 534 eV and redistributed spectral weight mainly between 537 and 540 eV (Fig. 4d). The changes near 532 and 534 eV correspond to the P=O π* and protonated P–OH environments, respectively, while the response above 536 eV contains higher energy phosphate and cation–oxygen states[21, 29]. These phosphate related changes show that water derived protons interact with SPO after assembly, while the principal Fe/Mo–O framework of SFM is retained.

Electrical conductivity relaxation then separated the effects of SPO on surface water exchange, oxygen diffusion and proton diffusion[25]. Following a switch from dry gas to pH_2O = 0.1 atm at 700 °C, SFM-SPO reached its characteristic response within 219 s, whereas SFM required 672 s (Fig. 4f). Fits across the measured temperature range yielded the surface water exchange coefficient, k_{H2O}, the oxygen chemical diffusion coefficient, D_O, and the proton chemical diffusion coefficient, D_H. SPO produced only modest changes in k_{H2O} and D_O, showing that neither surface water incorporation nor oxygen transport was substantially accelerated (Fig. 4g,h). By contrast, D_H increased from the low 10^{-6} cm^2 s^{-1} range in SFM to the 10^{-5} cm^2 s^{-1} range in SFM-SPO, an increase of nearly one order of magnitude (Fig. 4i). The dominant increase in D_H identifies accelerated proton transport as the origin of the lower polarization resistance and higher electrolysis performance in Fig. 3, rather than increased hydration capacity or modified oxygen transport[29].

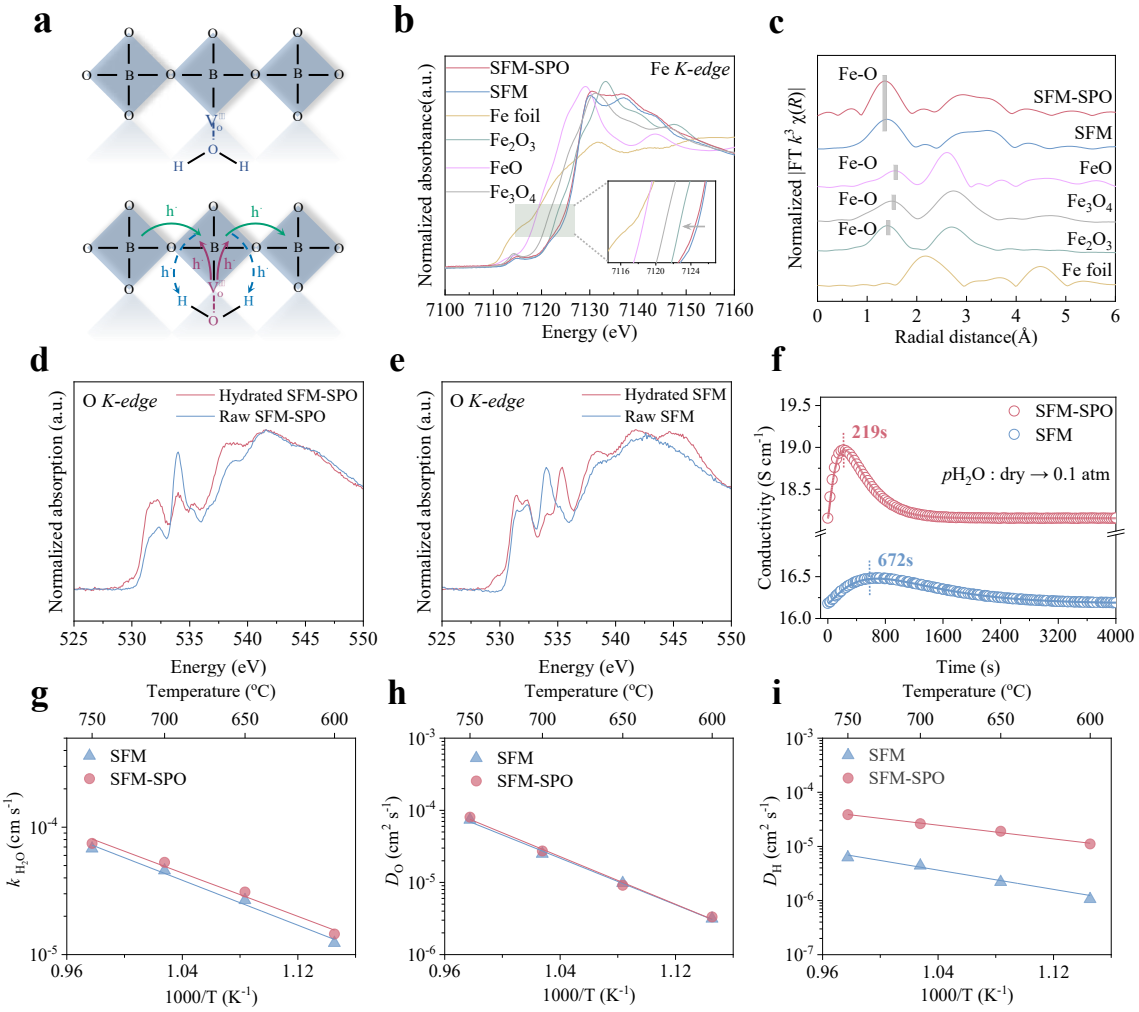


Fig. 4 | Selective acceleration of proton transport by SPO in the SFM composite. a, Schematic of water incorporation and proton transport in a proton-conducting perovskite oxide. b, Fe K edge XANES spectra of SFM, SFM-SPO and Fe reference compounds. c, Fourier transformed Fe K edge EXAFS spectra. d,e, Normalized O K edge spectra of dry and hydrated SFM-SPO (d) and SFM (e). f, Electrical conductivity relaxation transients following a change from dry gas to pH$_2$O = 0.1 atm at 700 °C. g-i, Surface water exchange coefficients, k_{H2O} (g), oxygen chemical diffusion coefficients, D_O (h), and proton chemical diffusion coefficients, D_H (i), from 600 to 750 °C.

Hydration thermodynamics in BZCYYb and SPO

The selective increase in D_H in SFM-SPO poses a materials question that cannot be resolved from the composite alone: does SPO improve proton transport by accommodating more protons, or by allowing a smaller proton population to move more freely? To separate proton formation from proton mobility, we compared isolated SPO with $BaZr_{0.1}Ce_{0.7}Y_{0.1}Y_{0.1}O_{3-\delta}$ (BZCYYb). BZCYYb provides a stringent benchmark because it is a widely used Ba(Ce,Zr)O_3 based proton conductor in which acceptor enabled hydration supplies a high proton

concentration and proton migration proceeds through a BO_6 octahedral framework[30, 31, 32]. Comparing the two materials therefore tests whether a PO_4 tetrahedral phosphate can establish a different balance between hydration thermodynamics and proton mobility. We first resolveed how BZCYYb and SPO interact with water and then determined how the incorporated protons move.

The contrasting hydration behaviour of BZCYYb and SPO begins with their different oxygen vacancy populations. Powder X-ray diffraction confirmed the expected crystal structures of both materials before hydration (Fig. 5a). Dry BZCYYb exhibited an intense oxygen vacancy related EPR signal near g = 2.00, which weakened after hydration, whereas SPO remained close to the baseline under both conditions (Fig. 5b)[33]. BZCYYb also showed a substantially larger mass loss in air than SPO (Fig. 5c). This mass loss reflects greater oxygen release and a higher oxygen vacancy content. The EPR and thermogravimetric results therefore establish that BZCYYb contains many more oxygen vacancy sites available for hydration than SPO.

The different oxygen vacancy populations produce distinct hydration responses in BZCYYb and SPO. Under pH_2O = 0.1 atm, BZCYYb developed a broad O–H stretching response between 300 and 500 °C, whereas SPO retained its characteristic phosphate vibrations without a comparable broad hydroxyl band (Fig. 5d,e)[34, 35]. The surface oxygen response followed the same contrast. Under humidified air containing 10 vol% H_2O at a total pressure of 1 mbar, corresponding to pH_2O = 0.1 mbar, the O 1s spectrum of BZCYYb contained components near 529 and 531 eV whose relative contributions changed with temperature (Fig. 5f)[36]. The higher binding energy component was assigned to hydroxyl containing species. SPO retained one dominant O 1s component over the same temperature range (Fig. 5g)[37]. BZCYYb therefore undergoes extensive vacancy mediated hydroxylation, whereas SPO does not form the same large hydroxyl population and largely preserves its phosphate oxygen environment.

The contrasting hydration behaviour has a thermodynamic origin. In BZCYYb, the calculated oxygen vacancy formation energy is 2.26 eV and the vacancy mediated hydration energy is -1.32 eV (Fig. 5h). Once an oxygen vacancy is present, its hydration is therefore energetically favourable. In SPO, the oxygen vacancy formation energy reaches 6.14 eV, which is 3.88 eV higher than that of BZCYYb (Fig. 5i)[38]. Water can therefore hydrate BZCYYb by filling oxygen vacancies, but this reaction is energetically inaccessible in the PO_4 framework of SPO. The proton population detected in SPO must instead arise from local interaction with phosphate oxygen without consuming a structural oxygen vacancy.

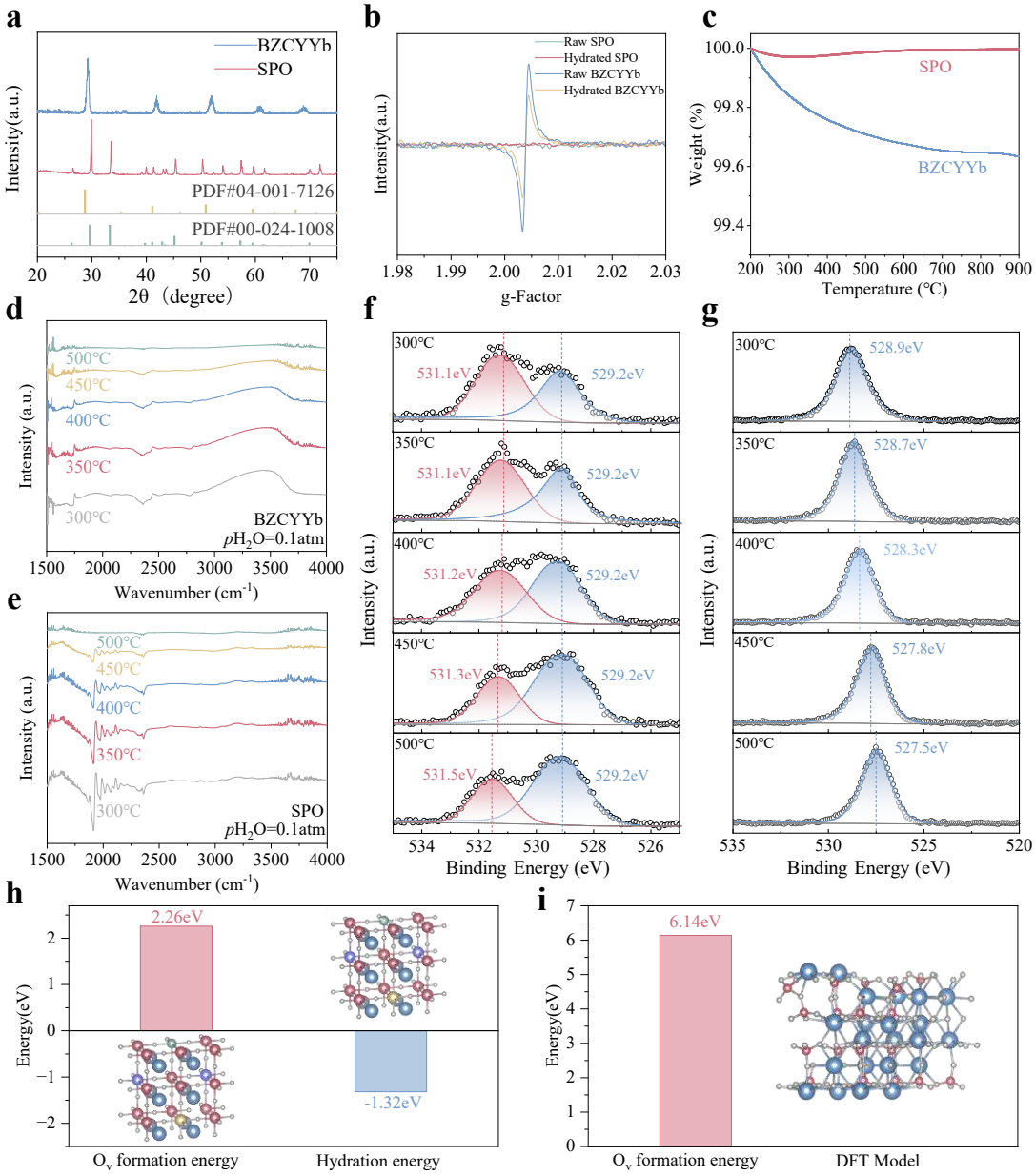


Fig. 5 | Hydration thermodynamics in BZCYYb and SPO. a, Powder X-ray diffraction patterns of BZCYYb and SPO. b, Electron paramagnetic resonance spectra of BZCYYb and SPO under dry and hydrated conditions at 400 °C. c, Thermogravimetric curves of BZCYYb and SPO. d, e, In situ infrared spectra of BZCYYb (d) and SPO (e) under pH_2O = 0.1 atm from 300 to 500 °C. f, g, Near ambient pressure O 1s X-ray photoelectron spectra of BZCYYb (f) and SPO (g). h, Calculated oxygen vacancy formation and vacancy mediated hydration energies for BZCYYb. i, Calculated oxygen vacancy formation energy and structural model of SPO.

Ultrafast proton migration between PO_4 tetrahedra in SPO

Because SPO forms a smaller proton population than BZCYYb, its contribution to electrode kinetics is expected to arise from greater proton mobility. TOF-SIMS was used to compare the isotope distributions after D_2O treatment at 600 °C and pD_2O = 0.1 atm for 30 min.

BZCYYb produced a much stronger D^+ signal, whereas SPO showed a lower overall intensity (Fig. 6a,b)[25]. The calibrated depth profiles, however, showed that the D^+ signal in BZCYYb decreased rapidly with depth, while SPO exhibited a slower relative attenuation and deeper isotope penetration (Fig. 6c)[39]. This slower attenuation indicates deeper deuterium penetration and faster isotope transport through the SPO phosphate sublattice.

The deeper isotope penetration in SPO is accompanied by a more dynamically active proton environment. Under identical acquisition conditions, solid-state ^{1}H NMR showed a broad and intense resonance for BZCYYb but a weaker and narrower resonance for SPO (Fig. 6d)[40]. The lower integrated intensity confirms the smaller proton population in SPO, while the narrower line reflects motional narrowing associated with faster local proton motion. Complementary ^{31}P MAS NMR identified the phosphate sites involved in this process. The SPO resonances near 2, 6 and 9 ppm were retained after hydration, while the envelope between 6 and 9 ppm broadened and developed an intermediate component (Supplementary Fig. S17)[41, 42]. This redistribution reflects local changes in P–O geometry caused by proton coupling to a fraction of the PO_4 tetrahedra[41]. SPO therefore contains a small but dynamically active proton population coupled directly to its phosphate structure.

Hydration couples the small mobile proton population in SPO directly to phosphate oxygen sites. In BZCYYb, hydration increased the low energy intensity near 532 eV, strongly redistributed the metal–oxygen hybridized feature around 534 eV and increased the broad spectral weight above 536 eV (Fig. 6e). These changes arise from vacancy filling, hydroxyl formation and the resulting redistribution of the Ce/Zr/Y/Yb–O electronic states[43]. SPO displayed a more localized response (Fig. 6f). Hydration changed the P=O π^* feature near 532 eV and the P–OH related region near 534 eV, while the broad P–O σ^* envelope above 536 eV retained its overall shape[21]. Together with ^{31}P NMR, these spectra locate the incorporated protons on PO_4 tetrahedra and distinguish local phosphate protonation from the extensive vacancy mediated hydroxylation observed in BZCYYb.

The arrangement of neighboring PO_4 tetrahedra provides the atomistic origin of the rapid proton motion identified by TOF-SIMS and NMR. In BZCYYb, the proton first reorients around a lattice oxygen atom and then transfers to a neighboring oxygen site within the BO_6 framework. The highest barrier along this pathway is about 0.35 eV (Fig. 6g and Supplementary Fig. S18)[44, 45]. In SPO, the proton reorients around an oxygen atom of one PO_4 tetrahedron before hopping to an oxygen atom on a neighboring tetrahedron. The rate limiting hop has a barrier of about 0.15 eV, only about 43% of the corresponding barrier in BZCYYb (Fig. 6h and Supplementary Fig. S19)[46, 47]. Rapid rotational diffusion followed by this low barrier transfer

enables ultrafast proton migration between adjacent PO_4 tetrahedra.

Together, these results establish SPO as an ultrafast proton conducting phosphate. BZCYYb incorporates more protons through vacancy mediated hydration, but acceptor defects create proton traps within its BO_6 framework. SPO contains fewer protons, yet its PO_4 tetrahedra provide a more uniform environment and a substantially lower migration barrier. SPO therefore enhances perovskite oxygen electrodes by introducing a distinct fast proton conducting material, rather than by further strengthening hydration in the oxide host. These results establish SPO as an ultrafast proton conducting phosphate for protonic ceramic oxygen electrodes.

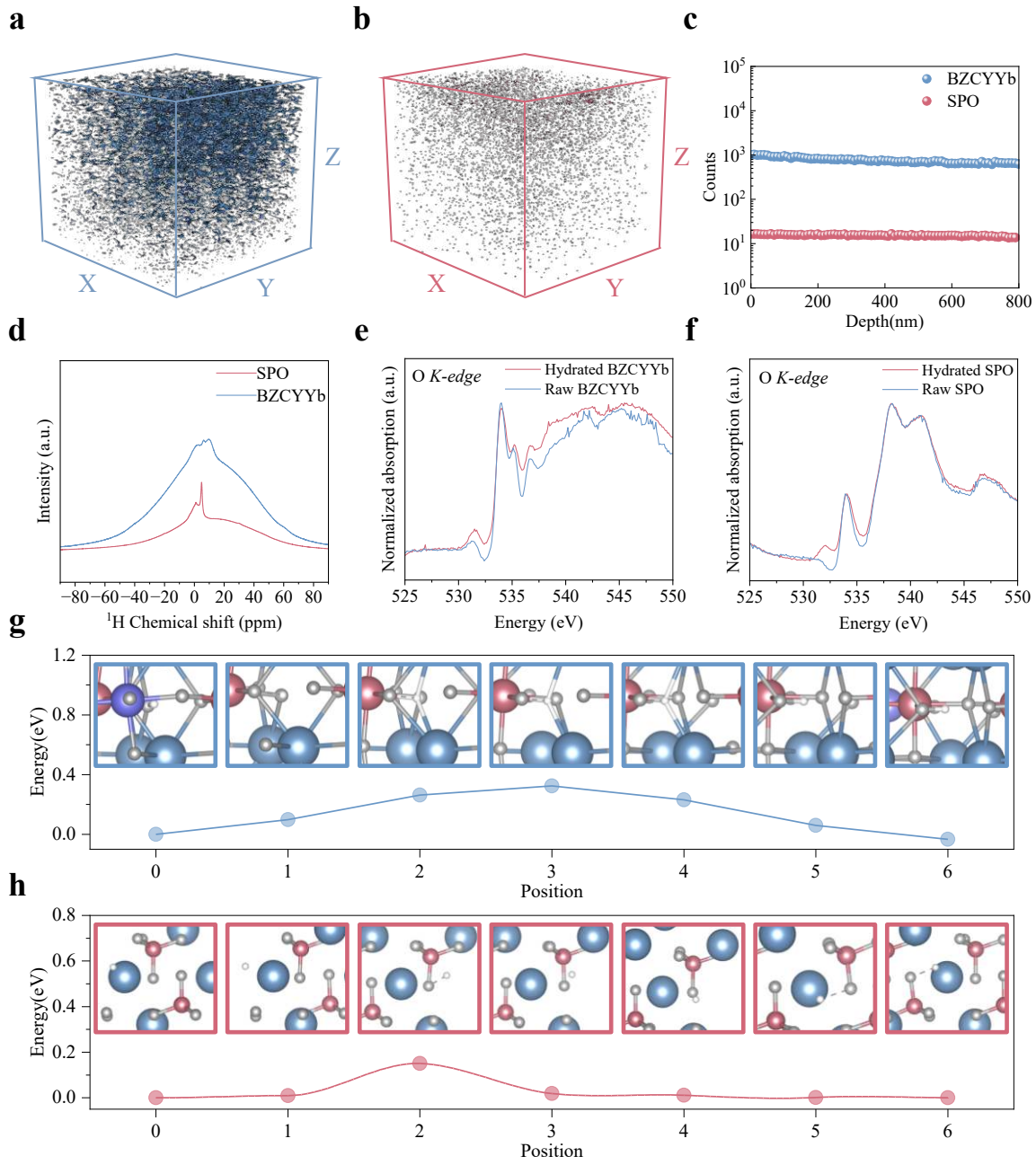


Fig. 6 | Ultrafast proton migration between PO_4 tetrahedra in SPO. a, b, Three-dimensional

TOF-SIMS reconstructions of D^+ distributions in BZCYYb (a) and SPO (b) after D_2O treatment. c, Corresponding D^+ depth profiles. d, Solid-state ^1H NMR spectra of BZCYYb and SPO after H_2O treatment. e, f, Normalized O K edge spectra of dry and hydrated BZCYYb (e) and SPO (f). g, h, Calculated proton migration paths and energy profiles in BZCYYb (g) and SPO (h).

Conclusion

We identify $Sr_3(PO_4)_2$ as a proton conducting material that operates outside the oxygen vacancy chemistry of conventional perovskite oxygen electrodes. Its PO_4 tetrahedral framework makes vacancy formation energetically costly and contains no acceptor dopants that can electrostatically trap protonic defects. The small proton population incorporated into SPO moves through rapid reorientation and a low barrier hop between oxygen atoms on neighboring tetrahedra. In situ self-assembly places the phosphate phase against the perovskite host. SFM-SPO retains the local Fe coordination, while its proton chemical diffusion coefficient rises by roughly one order of magnitude. The same strategy lowers polarization resistance and raises electrolysis current density in SFN, SCF and SCN. SPO therefore changes the structural basis of proton transport instead of further tuning vacancy related traps within the oxide lattice. These results establish an independent phosphate pathway for accelerating proton transport in protonic ceramic oxygen electrodes.

Methods

Materials synthesis

$Sr_3(PO_4)_2$ (SPO) was obtained by a solid-state route from stoichiometric $SrCO_3$ and $NH_4H_2PO_4$. After 24 h of dry milling, the mixture was heated in air at 600 °C for 2 h. The product was reground and fired again at 1,400 °C for 5 h.

$BaZr_{0.1}Ce_{0.7}Y_{0.1}Yb_{0.1}O_{3-\delta}$ (BZCYYb) was prepared from stoichiometric BaO, ZrO_2, CeO_2, Y_2O_3 and Yb_2O_3. The oxides were ball milled for 72 h and calcined in air at 1,100 °C for 10 h. After regrinding, the same calcination step was repeated.

A sol-gel combustion process produced the four electrode compositions and their SPO-containing variants. Each solution contained the required stoichiometric amounts of $Sr(NO_3)_2$, $Fe(NO_3)_3{\cdot}9H_2O$, $Co(NO_3)_2{\cdot}6H_2O$, $(NH_4)_6Mo_7O_{24}{\cdot}4H_2O$, ammonium niobium oxalate and $NH_4H_2PO_4$. Total metal ions, glycine and citric acid were combined at a molar ratio of 1.5:1:1. Stirring at 80 °C converted the solution into a yellow gel. The gel was heated at 250 °C with sufficient aeration to form a black precursor, which was subsequently calcined in air at 1,100 °C for 5 h.

Structural and chemical characterization

Powder X-ray diffraction patterns were recorded on an X'Pert Pro MPD instrument using Cu Kα radiation at 40 kV and 40 mA. GSAS was used for Rietveld refinement. For variable temperature diffraction, the sample was held in air for 10 min at each 50 °C step between 400 and 700 °C before data collection. An FEI Tecnai F20 microscope operated at 200 kV provided the EDX, HRTEM and SAED data. Mass changes in flowing air at 100 ml min^{-1} were recorded on a Netzsch STA 449 F5 at a heating rate of 5 °C min^{-1}. A VG MultiLab 2000 system was used for laboratory XPS.

EPR spectra were recorded at 9 GHz with 100 kHz modulation on a Bruker E500. Dry and humidified specimens were conditioned for 0.5 h at 400 °C. Humidification used 10 vol% H_2O at a total flow of 100 ml min^{-1}.

In situ diffuse reflectance infrared Fourier transform spectroscopy

DRIFTS measurements used a Bruker VERTEX 80v. Ar carrying 10 vol% water vapour flowed over the sample at 100 ml min^{-1}. After 30 min equilibration at 300, 350, 400, 450 and 500 °C, 32 scans were averaged from 4,000 to 400 cm^{-1} at a resolution of 4 cm^{-1}.

Near ambient pressure X-ray photoelectron spectroscopy

Near ambient pressure X-ray photoelectron spectroscopy was performed using a SPECS NAP-XPS Backfilling system. About 60 mg of each powder was pelletized and attached to the laser heated holder. The sample entered the analysis chamber after evacuation of the load lock to 1×10^{-8} mbar. Once the analysis chamber reached 1×10^{-9} mbar, humidified air containing 10 vol% H_2O was supplied at 100 ml min^{-1}. The total pressure was held at 1 mbar, giving pH_2O = 0.1 mbar. Measurements were made from 300 to 500 °C after 10 min equilibration at each temperature. A monochromatic Al Kα source at 15 kV and 20 W was used to acquire high resolution O 1s and C 1s spectra in 0.1 eV steps. Binding energies were referenced to adventitious C 1s at 284.8 eV. CasaXPS fits used a Shirley background and GL(30) Gaussian-Lorentzian line shapes.

Synchrotron soft X-ray spectroscopy

TEY O K-edge spectra were measured at the BL10B photoemission spectroscopy beamline (31131.02.HLS.PES), National Synchrotron Radiation Laboratory, Hefei. BL10B covers photon energies from 100 to 1,100 eV with E/ΔE greater than 1,000. Dry and hydrated BZCYYb, SPO, SFM and SFM-SPO samples were loaded together. Hydration was carried out at 600 °C for 30 min under pH_2O = 0.1 atm at a total flow of 100 ml min^{-1}. Before collection, the complete batch remained under vacuum at room temperature for 3 h. TEY was recorded from the sample compensation current. Incident photon flux correction preceded alignment to a shared energy reference and normalization against the post edge intensity. The hydrated minus

dry difference was calculated from the normalized spectra. Data were acquired between 520 and 560 eV in 0.1 eV increments.

XANES and EXAFS

Fe K-edge spectra were recorded in transmission on a SuperXAFS H3000 laboratory instrument. The first inflection point of Fe foil at 7,112 eV defined the energy scale. Athena handled data processing, and Artemis was used for fitting. Fits covered k = 3 to 12 $Å^{-1}$ and R = 1.0 to 3.5 Å, with a Hanning window and $S_0^2 = 0.9$.

Solid-state NMR and isotope tracing

Solid-state $^{1}H/^{31}P$ NMR measurements used a Bruker Avance Neo 400WB. Samples were humidified at 600 °C for 30 min under $pH_2O = 0.1$ atm and a total flow of 100 ml min^{-1}. Spectra were acquired in a 4 mm zirconia rotor at 10 kHz MAS using a single pulse, a 5 s recycle delay and 128 scans. Chemical shifts were referenced to tetramethylsilane at 0 ppm. Dry and hydrated SPO were examined by solid state ^{31}P MAS NMR on the same instrument. The 4 mm rotor spun at 10 kHz. A single 90° pulse, a 5 s recycle delay and 256 scans were used. The external reference was 85% H_3PO_4 at 0 ppm.

D_2O exchange was performed at 600 °C for 30 min in Ar/O_2 containing $pD_2O = 0.1$ atm. The carrier contained 21 vol% O_2 and flowed at 100 ml min^{-1}. A PHI nano TOF II recorded the D^+ depth profiles using a 30 kV Bi^{3+} analysis beam and a 3 kV, 100 mA Ar^+ sputtering beam. The analysis and sputtering areas were 40 × 40 nm^2 and 400 × 400 nm^2, respectively.

Electrical conductivity relaxation

SFM and SFM-SPO were pressed into 2 × 4 × 10 mm bars and sintered at 1,100 °C for 2 h, giving relative densities above 95%. Four probe d.c. conductivity and ECR data were obtained with a Keithley 2400 source meter. Between 600 and 750 °C, the atmosphere was changed from dry to humidified Ar/O_2 with $pH_2O = 0.1$ atm. Both streams contained 21 vol% O_2 and flowed at 100 ml min^{-1}. Recording continued until equilibrium. The normalized transients were fitted with the rectangular bar solution to Fick's second law under finite surface exchange conditions to extract k_{H2O}, D_O and D_H.

Cell fabrication and electrochemical measurements

Dense BZCYYb electrolyte substrates were prepared by dry pressing and sintered at 1450 °C for 5 h. Symmetric cells were prepared by screen printing oxygen electrode slurries on both sides of the electrolyte and calcining in air at 1100 °C for 2 h. Silver paste was used as the current collector.

Fuel electrode supported cells were prepared with a NiO-BZCYYb | BZCYYb | oxygen electrode configuration. Impedance was recorded on a PARSTAT 2273 from 10^5 to 10^{-2} Hz

using a 10 mV perturbation. Electrolysis current-voltage curves were measured from 500 to 700 °C at 10 mV s^{-1}. The fuel side received equal volumes of H_2 and Ar at 100 ml min^{-1}, while air containing 10 vol% H_2O flowed over the oxygen electrode at the same rate. Polarization resistance was taken as the separation between the high and low frequency intercepts on the real impedance axis.

DFT calculations

All DFT calculations used the Vienna Ab initio Simulation Package. Exchange and correlation were treated within the PBE generalized gradient approximation using projector augmented wave potentials. The plane wave cutoff was 450 eV. Spin polarization and DFT-D3 dispersion corrections were included. Electronic energies converged to 10^{-5} eV, and structures were relaxed until every residual force was below 0.05 eV $Å^{-1}$.

A 15 Å vacuum gap separated periodic images along the BZCYYb slab normal. During relaxation, the lower third of the slab was fixed and all remaining atoms could move. The BZCYYb and SPO Brillouin zones were sampled with 2 × 1 × 1 and 4 × 2 × 1 Monkhorst-Pack meshes, respectively.

The oxygen vacancy formation energy was calculated as

$$E_{ovf} = E_{defective} + 1/2E_{O2} - E_{pristine},$$

Here, $E_{defective}$ and $E_{pristine}$ denote the energies of the oxygen deficient and pristine models, and E_{O2} is the energy of an isolated O_2 molecule.

The vacancy mediated hydration energy was calculated as

$$E_{hydr} = E_{hydrated} - E_{vacancy} - E_{H2O},$$

Here, $E_{hydrated}$ and $E_{vacancy}$ denote the hydrated and vacancy containing models, while E_{H2O} is the energy of an isolated H_2O molecule.

Migration barriers were obtained with the climbing image nudged elastic band method. Each path comprised two endpoints and five intermediate images. Transition state optimization used the same force threshold of 0.05 eV $Å^{-1}$.

References

1. Choi S, Kucharczyk CJ, Liang Y, Zhang X, Takeuchi I, Ji H-I*, et al.* Exceptional Power Density and Stability at Intermediate Temperatures in Protonic Ceramic Fuel Cells. *Nature Energy* 2018, **3**(3)**:** 202-210.

2. Tsujikawa K, Hyodo J, Fujii S, Takahashi K, Tomita Y, Shi N*, et al.* Mitigating proton trapping in cubic perovskite oxides via ScO_6 octahedral networks. *Nature Materials* 2025, **24**(12)**:** 1949-1956.

3. Yamazaki Y, Blanc F, Okuyama Y, Buannic L, Lucio-Vega JC, Grey CP*, et al.* Proton trapping in yttrium-doped barium zirconate. *Nature Materials* 2013, **12**(7)**:** 647-651.

4. Kreuer KD. Proton-Conducting Oxides. *Annual Review of Materials Research* 2003, **33**(Volume 33, 2003)**:** 333-359.

5. Kreuer KD. Aspects of the formation and mobility of protonic charge carriers and the stability of perovskite-type oxides. *Solid State Ionics* 1999, **125**(1)**:** 285-302.

6. Iwahara H, Esaka T, Uchida H, Maeda N. Proton conduction in sintered oxides and its application to steam electrolysis for hydrogen production. *Solid State Ionics* 1981, **3-4:** 359-363.

7. Duan C, Tong J, Shang M, Nikodemski S, Sanders M, Ricote S*, et al.* Readily Processed Protonic Ceramic Fuel Cells with High Performance at Low Temperatures. *Science* 2015, **349**(6254)**:** 1321-1326.

8. Yang L, Wang S, Blinn K, Liu M, Liu Z, Cheng Z*, et al.* Enhanced Sulfur and Coking Tolerance of a Mixed Ion Conductor for SOFCs: $BaZr_{0.1}Ce_{0.7}Y_{0.2-x}Yb_xO_{3-\delta}$. *Science* 2009, **326**(5949)**:** 126-129.

9. Wang X, Cai Z, Chen Z, Liu D, Chen W, Zhu J*, et al.* Highly ionic-dispersed oxygen electrode for reversible proton ceramic electrochemical cells. *Nature Communications* 2026, **17**(1)**:** 3989.

10. Song Y, Chen Y, Wang W, Zhou C, Zhong Y, Yang G*, et al.* Self-Assembled Triple-Conducting Nanocomposite as a Superior Protonic Ceramic Fuel Cell Cathode. *Joule* 2019, **3**(11)**:** 2842-2853.

11. Ding H, Wu W, Jiang C, Ding Y, Ding D. Self-sustainable protonic ceramic electrochemical cells using a triple conducting electrode for hydrogen and power production. *Nature Communications* 2020, **11**(1).

12. Zheng H, Riegraf M, Sata N, Costa R. A double perovskite oxygen electrode in Zr-rich proton conducting ceramic cells for efficient electricity generation and hydrogen production. *Journal of Materials Chemistry A* 2023, **11**(20)**:** 10955-10970.

13. Løken A, Bjørheim TS, Haugsrud R. The pivotal role of the dopant choice on the thermodynamics of hydration and associations in proton conducting $BaCe_{0.9}X_{0.1}O_{3-\delta}$ (X = Sc, Ga, Y, In, Gd and Er). *Journal of Materials Chemistry A* 2015, **3**(46)**:** 23289-23298.

14. Kruth A, Irvine JTS. Water incorporation studies on doped barium cerate perovskites. *Solid State Ionics* 2003, **162-163:** 83-91.

15. Shin Y, Doh K-Y, Lee JH, Kim SH, Lee D. Synergistic Interplay of Acceptor and Isovalent Co-Doping on $BaZrO_3$-Based Proton Conducting Oxides: A First-Principles Study. *Advanced Science* 2026, **13**(30)**:** e24188.

16. Zheng S, Wu W, Zhang Y, Zhao Z, Duan C, Karki S*, et al.* Enhancing surface activity and durability in triple conducting electrode for protonic ceramic electrochemical cells. *Nature Communications* 2025, **16**(1)**:** 4146.

17. Ren R, Wang Z, Meng X, Wang X, Xu C, Qiao J*, et al.* Tailoring the Oxygen Vacancy to Achieve Fast Intrinsic Proton Transport in a Perovskite Cathode for Protonic Ceramic Fuel Cells. *ACS Applied Energy Materials* 2020, **3**(5)**:** 4914-4922.

18. Song L, Qiao Y, Zhao Y, Ren R, Wang Z, Jia C*, et al.* Accelerating Bulk Proton Transfer in $Sr_2Fe_{1.5}Mo_{0.5}O_{6-\delta}$ Perovskite Oxide for Efficient Oxygen Electrode in Protonic Ceramic Electrolysis Cells. *Ceramics International* 2024, **50**(14)**:** 24987-24994.

19. Ren R, Sun J, Wang G, Xu C, Qiao J, Sun W*, et al.* Rational design of $Sr_2Fe_{1.5}Mo_{0.4}Y_{0.1}O_{6-\delta}$ oxygen electrode with triple conduction for hydrogen production in protonic ceramic electrolysis cell. *Separation and Purification Technology* 2022, **299:** 121780.

20. Xiaojie C, Guangdong L, Rongzheng R, Chunming X, Jinshuo Q, Wang S*, et al.* Improving Performance of Proton Ceramic Electrolysis Cell Perovskite Anode by Zn Doping. *Ceramics International* 2023, **49**(12)**:** 19879-19884.

21. Nagasaka M, Kumaki F, Adachi J-i. Double-Bond Character of Phosphates in Solid and Liquid Phases Probed by Oxygen K-Edge X-ray Absorption Spectroscopy. *The Journal of Physical Chemistry Letters* 2026, **17**(23)**:** 6432-6437.

22. Abbate M, De Groot F, Fuggle J, Fujimori A, Strebel O, López M*, et al.* Controlled-valence properties of $La_{1-x}Sr_xFeO_3$ and $La_{1-x}Sr_xMnO_3$ studied by soft-x-ray absorption spectroscopy. *Physical Review B* 1992, **46:** 4511-4519.

23. Suntivich J, May KJ, Gasteiger HA, Goodenough JB, Shao-Horn Y. A Perovskite Oxide Optimized for Oxygen Evolution Catalysis from Molecular Orbital Principles. *Science* 2011, **334**(6061)**:** 1383-1385.

24. Chen X, Tan Y, Li Z, Liu T, Song Y, Zhai S*, et al.* Advanced Air Electrodes for Reversible Protonic Ceramic Electrochemical Cells: A Comprehensive Review. *Advanced Materials* 2025, **37**(48)**:** 2418620.

25. Seong A, Kim J, Jeong D, Sengodan S, Liu M, Choi S*, et al.* Electrokinetic Proton Transport in Triple ($H^+/O^{2-}/e^-$) Conducting Oxides as a Key Descriptor for Highly Efficient Protonic Ceramic Fuel Cells. *Advanced Science* 2021, **8**(11)**:** 2004099.

26. Grimaud A, Diaz-Morales O, Han B, Hong WT, Lee Y-L, Giordano L*, et al.* Erratum: Activate lattice oxygen redox reactions in metal oxides to catalyse oxygen evolution. *Nature Chemistry* 2018, **10**(2)**:** 242-242.

27. Björketun ME, Sundell PG, Wahnström G. Structure and thermodynamic stability of hydrogen interstitials in $BaZrO_3$ perovskite oxide from density functional calculations. *Faraday Discussions* 2007, **134:** 247-265.

28. Yamazaki Y, Yang C-K, Haile SM. Unraveling the defect chemistry and proton uptake of yttrium-doped barium zirconate. *Scripta Materialia* 2011, **65**(2)**:** 102-107.

29. Yoo H-I, Kim J-K, Lee C-E. Electrical Conductivity Relaxations and Chemical Diffusivities of $BaCe_{0.95}Yb_{0.05}O_{2.975}$ upon Hydration and Oxidation. *Journal of The Electrochemical Society* 2008, **156**(1)**:** B66.

30. Liu Z, Song Y, Xiong X, Zhang Y, Cui J, Zhu J*, et al.* Sintering-induced cation displacement in protonic ceramics and way for its suppression. *Nature Communications* 2023, **14**(1)**:** 7984.

31. Draber FM, Ader C, Arnold JP, Eisele S, Grieshammer S, Yamaguchi S*, et al.* Nanoscale percolation in doped $BaZrO_3$ for high proton mobility. *Nature Materials* 2020, **19**(3)**:** 338-346.

32. Kjølseth C, Wang L-Y, Haugsrud R, Norby T. Determination of the enthalpy of hydration of oxygen vacancies in Y-doped $BaZrO_3$ and $BaCeO_3$ by TG-DSC. *Solid State Ionics* 2010, **181**(39)**:** 1740-1745.

33. Ahmed I, Eriksson SG, Ahlberg E, Knee CS, Götlind H, Johansson LG*, et al.* Structural study and proton conductivity in Yb-doped $BaZrO_3$. *Solid State Ionics* 2007, **178**(7)**:** 515-520.

34. Naumovska E, Nzulu GK, Mazzei L, Le Febvrier A, Komander K, Magnuson M*, et al.* Local structure of hydrated nanocrystalline films of the proton conductor $BaZr_{1-x}Sc_xO_{3-x/2}$ studied by infrared spectroscopy. *Vibrational Spectroscopy* 2024, **130:** 103622.

35. Eichel R-A. Structural and dynamic properties of oxygen vacancies in perovskite oxides—analysis of defect chemistry by modern multi-frequency and pulsed EPR techniques. *Physical Chemistry Chemical Physics* 2011, **13**(2)**:** 368-384.

36. Jarry A, Jackson GS, Crumlin EJ, Eichhorn B, Ricote S. The effect of grain size on the hydration of $BaZr_{0.9}Y_{0.1}O_{3-\delta}$ proton conductor studied by ambient pressure X-ray photoelectron spectroscopy. *Physical Chemistry Chemical Physics* 2020, **22**(1)**:** 136-143.

37. Zhao Z, Ling X, El Gabaly F, Grass M, Jabeen N, Jones D*, et al.* Observation of Potential-Induced Hydration on the Surface of Ceramic Proton Conductors Using In Situ Near-Ambient Pressure X-ray Photoelectron Spectroscopy. *The Journal of Physical Chemistry Letters* 2022, **13**(13)**:** 2928-2933.

38. Takahashi H, Yashima I, Amezawa K, Eguchi K, Matsumoto H, Takamura H*, et al.* First-Principles Calculations for the Energetics of the Hydration Reaction of Acceptor-Doped $BaZrO_3$. *Chemistry of Materials* 2017, **29**(4)**:** 1518-1526.

39. De Souza RA, Zehnpfenning J, Martin M, Maier J. Determining oxygen isotope profiles in oxides with Time-of-Flight SIMS. *Solid State Ionics* 2005, **176**(15)**:** 1465-1471.

40. Buannic L, Sperrin L, Dervişoğlu R, Blanc F, Grey CP. Proton distribution in Sc-doped $BaZrO_3$: a solid state NMR and first principle calculations analysis. *Physical Chemistry Chemical Physics* 2018, **20**(6)**:** 4317-4328.

41. Olivieri A. A Correlation between ^{31}P NMR chemical-shift tensors in solid phosphates and P-O bond lengths. Implications for proton transfer processes. *Journal of Magnetic Resonance (1969)* 1990, **88**(1)**:** 1-8.

42. Gardiennet C, Henry B, Kuad P, Spiess B, Tekely P. Straightforward detection of the secondary ionisation of the phosphate group and pK determinations by high-resolution solid-state ^{31}P NMR. *Chemical Communications* 2005, **41**(2)**:** 180-182.

43. Frati F, Hunault MOJY, de Groot FMF. Oxygen K-edge X-ray Absorption Spectra. *Chemical Reviews* 2020, **120**(9)**:** 4056-4110.

44. Henkelman G, Uberuaga BP, Jónsson H. A Climbing Image Nudged Elastic Band Method for Finding Saddle Points and Minimum Energy Paths. *The Journal of Chemical Physics* 2000, **113**(22)**:** 9901-9904.

45. Merinov B, Goddard W, III. Proton diffusion pathways and rates in Y-doped $BaZrO_3$ solid oxide electrolyte from quantum mechanics. *The Journal of Chemical Physics* 2009, **130**(19).

46. Vilčiauskas L, Tuckerman ME, Bester G, Paddison SJ, Kreuer K-D. The mechanism of proton conduction in phosphoric acid. *Nature Chemistry* 2012, **4**(6)**:** 461-466.

47. Li Z, Lin Y, Garaga MN, Greenbaum SG, Liao M, Ruan J*, et al.* Quantitative and mechanistic insights into proton dynamics for fast energy storage. *Nature Materials* 2025, **24**(12)**:** 1968-1977.

Acknowledgements

This work was supported by the National Natural Science Foundation of China (Grant No. 52202208). We thank the staff members of the BL10B (nltps://cstr.cn/31131.02.HLS.PES) at the National SynchrotronRadiation Laboratory in Hefei (https://cstr.cn/ 31131.02.HLS), for providing technical supportand assistance in data collection and analysis.

Supplementary Files

This is a list of supplementary files associated with this preprint. Click to download.

- SupportingInformation.docx